Effects of Gravity on Foam Behavior in Roughened Model Fractures

Li, K.; Wolf, K. A. A.; Rossen, W. R.

DOI
10.2118/206735-PA

Publication date
2021

Document Version
Final published version

Published in
SPE Journal

Effects of Gravity on Foam Behavior in Roughened Model Fractures

K. Li*, K. A. A. Wolf, and **W. R. Rossen,** Delft University of Technology

Summary

In this study, to investigate how gravity affects foam in open vertical fractures, we report foam experiments in three 1-m-long, 15-cm-wide glass-model fractures. Each fracture has a smooth wall and a roughened wall. Between the two walls is a slit-like channel representing a single geological fracture. Three model fractures (Models A, B, and C) share the same roughness and have different hydraulic apertures of 78, 98, and 128 μm, respectively. We conduct foam experiments by horizontal injection in the three model fractures placed horizontally and sideways (i.e., with the model fractures turned on their long side), and in Model A placed vertically with injection upward or downward. Direct imaging of the foam inside the model fracture is facilitated using a high-speed camera. We find that foam reaches local equilibrium (LE; where the rate of bubble generation equals that of bubble destruction) in horizontal-flow experiments in all three model fractures and in vertical-flow experiments in Model A. In fractures with a larger hydraulic aperture, foam is coarser because of less in-situ foam generation. In the vertical-flow experiments in Model A, we find that the properties of the foam are different in upward and downward flow. Compared with downward flooding, upward flooding creates a finer-texture foam, as sections near the inlet of this experiment are in a wetter state, which benefits in-situ foam generation. Moreover, less gas is trapped during upward flooding, as gravitational potential helps overcome the capillarity and moves bubbles upward. In the sideways-flow experiments, gravity segregation takes place. As a result, drier foam propagates along the top of the fractures and wetter foam along the bottom. The segregation is more significant in fractures with a larger hydraulic aperture. At foam quality 0.8, gas saturation is 27.7% greater at the top than the bottom for Model C, and 19.3% and 10.8% for Models B and A, respectively. Despite the gravity segregation in all three model fractures, water and gas are not completely segregated. All three model fractures thus represent a capillary transition zone, with greater segregation with increasing aperture. Our results suggest that the propagation of foam in vertical natural fractures meters tall and tens of meters long, with an aperture of hundreds of microns or greater, is problematic. Gravity segregation in foam would weaken its capacity in the field to maintain uniform flow and divert gas in a tall fracture over large distances.

Introduction

Naturally fractured reservoirs (NFRs) gain much attention worldwide because of their large reserves of hydrocarbons (Persoff and Pruess 1995). However, oil recovery by gas injection in NFRs is usually low because of poor sweep efficiency. During gas injection, the displacement front is unstable. Conformance problems, such as gravity override and viscous fingering, occur because the gas has a lighter density and lower viscosity compared with reservoir fluids. In addition, open fractures can have an aperture of hundreds of microns or more (Luthi and Souhaite 1990), with a conductivity much greater than the matrix. As a result, gas flows through fractures, leaving much of the matrix unswept.

Foam, composed of gas bubbles separated by surfactant-contained films (lamellae), has many applications in underground resources, such as acid stimulation (Thompson and Gdanski 1993), aquifer remediation (Hirasaki et al. 1997), and enhanced oil recovery (Kovscek and Radke 1994; Rossen 1996). In enhanced oil recovery, foam can effectively mitigate conformance problems by reducing the mobility of gas by a factor of hundreds or more (Tang and Kovscek 2006). During foam flooding, the displacement front is more stable, and more gas is diverted to unswept zones, hence improving sweep, reducing the gas/oil ratio, and increasing oil recovery (Patzek 1996).

In the laboratory, foam can also be created inside fractures with various geometries (Fernø et al. 2016; AlQuaimi and Rossen 2019a; Brattekås et al. 2020). In fractures, foam can build up a viscous pressure gradient and thus divert the flow of gas into the matrix. As a result, the sweep is improved (Farajzadeh et al. 2010). In the tight, fractured reservoir in Woodbine, Katiyar et al. (2019) reported an immiscible hydrocarbon foam pilot. The injection strategy of surfactant-alternating-gas was adopted. They observed an increased oil-production rate and an increased gas-utilization ratio. Foam was also successfully implemented in the naturally-fractured gas-condensate Piedemonte Field (Ocampo et al. 2020). By dispersing the surfactant solution in the hydrocarbon gas, a delayed gas breakthrough and a reduction of the gas/oil ratio were achieved.

Despite the success, foam application in NFRs is still less understood. In NFRs, fractures are created by earth stresses. They have different conductivity, volume, and roughness (van Golf-Racht 1982). Usually associated with folds, natural fractures can be meters tall and tens of meters long. In most NFRs, principle stresses (in parallel with the horizontal plane) are smaller than overburden pressure. Thus, fractures are inclined with a dip angle larger than 60° or even vertical (Stearns and Friedman 1972). All these complexities of fractures can significantly affect flow dynamics in NFRs.

In this study, we report a series of foam experiments in three 1-m-long model fractures with different hydraulic apertures to investigate the effects of gravity on foam. We conduct the experiments by placing the fractures horizontally, vertically, and sideways. The model fractures are made of glass plates. Their transparency allows for direct visualization of foam using a high-speed camera.

In this paper, we describe our experimental setup and model fractures. Then we characterize the roughened surface of the fractures and explain how foam texture and gas saturation are quantified in our fractures. We further show how foam behaves in all three fractures and we discuss how the hydraulic aperture of the fracture affects the foam strength. In addition, we examine the effects of gravity on foam in sideways-placed fractures and we report how gas saturation varies at different heights of the fracture. We also compare how the influence of gravity differs between three model fractures with different hydraulic apertures.

*Corresponding author; email: K.Li-2@tudelft.nl

Original SPE manuscript received for review 17 April 2021. Revised manuscript received for review 11 June 2021. Paper (SPE 206735) peer approved 29 June 2021.

Experimental Setup and Materials

Fig. 1 shows the experimental setup. A mass-flow controller is used to inject gas, and a pump is used to inject liquids. Seven absolute-pressure transducers measure the pressure at different locations along the model fracture. A computer regulates the injection rates of the mass-flow controller and the pump, and also record pressure measurements, from which the pressure gradient can also be computed. A detailed description of the setup has been reported elsewhere (Li et al. 2021).

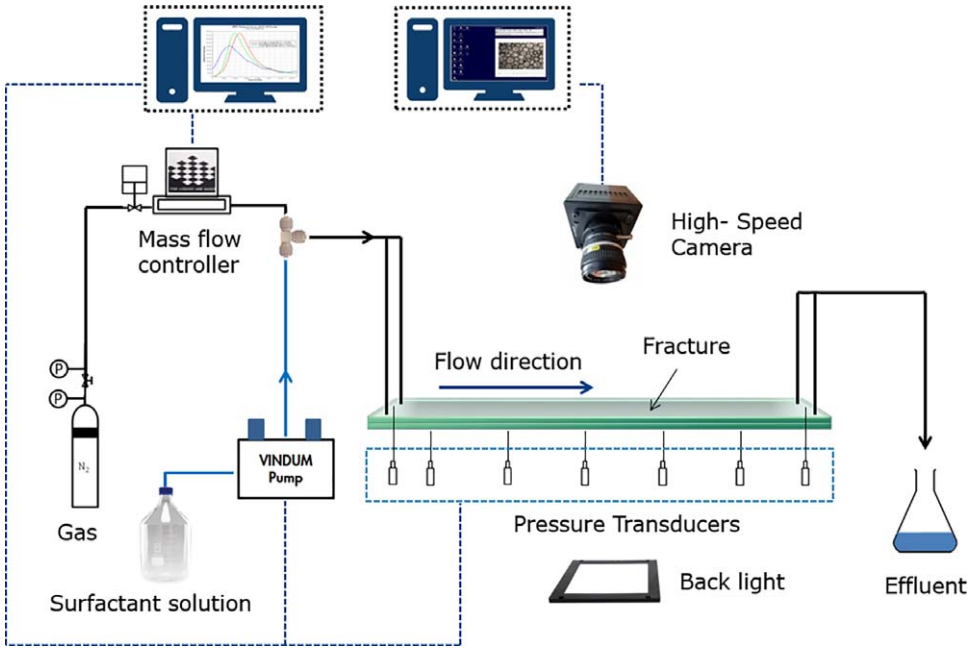

Fig. 1—Experimental setup.

In this study, we build three model fractures: Models A, B, and C. The three model fractures have the same dimensions (length×width: 1×0.15 m), but different hydraulic apertures. Each model fracture consists of two glass plates (Hijman Glas B.V., Rijswijk, The Netherlands). One plate is smooth and the other one is rough on the side facing the other plate. Both plates are 2 cm thick.

To create Model A, the two glass plates are placed directly against each other, and sealed along edges with silicone rubber glue (RESIN Products & Technology B.V., Enschede, The Netherlands). The model is then mounted inside an aluminum clamping frame **(Fig. 2).** The space between the two glass plates represents the aperture of the fracture. We disassemble Model A after we perform all experiments on this fracture and use the same roughened plate to create Model B, using the same procedures. We also use the same roughened plate to create Model C after completing experiments on Model B. All three model fractures thus share the same roughness. However, in Models B and C, 3-mm-wide strips of copper foil (with thickness of 25 and 75 μm, respectively) are placed along the edges between the two plates to increase the aperture of the fractures.

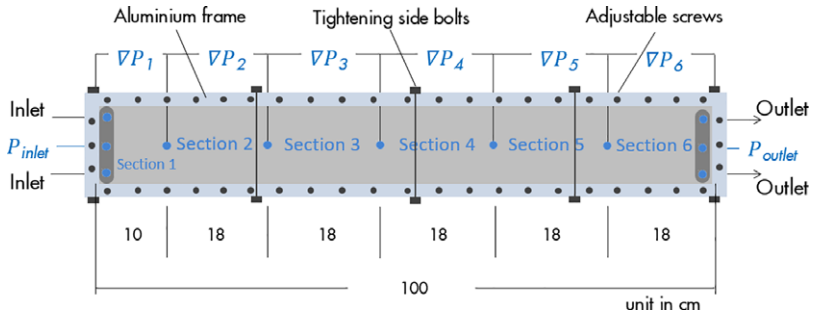

Fig. 2—Assembly of the model fracture (top view of the horizontally-placed fracture).

For each model fracture, 11 holes are drilled through the roughened plate for foam injection and production and connection to the pressure transducers (Fig. 2). The 1-m-long model fracture is divided into six sections. Two troughs (length×width×depth: $12 \times 2 \times 0.04$ cm) are engraved on the roughened plate. The inlet trough helps foam flow evenly into the fracture. The outlet trough prevents foam from converging near the end of the fracture.

In this study, a high-speed camera (Photron Fastcam® UX50, Tokyo, Japan; up to 160,000 fps), mounted perpendicular to the fracture plane, is used to capture the foam process in the fractures (Fig. 1). At the opposite side of the fracture, a high-parallelism chip backlight device (Model VL-CB0909W-CL, VS Technology Machine Vision Optics, Tokyo, Japan) is mounted to provide stable white light for the camera. A computer operates the camera and handles image acquisition. The whole setup is placed inside a tent to avoid external reflections to improve the quality of images.

In this study, 1 wt% alpha olefin sulfonate (AOS) C14-16 surfactant solution (Stepan BIO-TERGE® AS-40 KSB, Northfield, Illinois, USA) and nitrogen (purity ≥ 99.999%; Linde Gas Benelux B.V., Schiedam, The Netherlands) are used to create foams.

Methodologies

Hydraulic Aperture and Volume of Model Fractures. The hydraulic apertures, d_H, of all three model fractures are computed before the foam experiments. We compute d_H by injecting demineralized water through the model (after first removing all gas) at stepwise-increasing rates. The pressure gradient during water injection at each rate is recorded after the steady-state condition has been reached. A regression of the pressure gradient against the injection rate determines d_H (Witherspoon et al. 1980),

$$\nabla P_w = 12\, q_w \frac{1}{w\, d_H^3}\, \mu_w, \quad (1)$$

where ∇P_w is the pressure gradient of the water injection, q_w is the volumetric rate of water injection, w is the width of the model fracture, and μ_w is water viscosity. The values of d_H obtained from Eq. 1 are 78, 98, and 128 μm for Models A, B, and C, respectively. The definition of d_H approximates the model fracture as a smooth slit. It is related to the permeability of the model fracture by (Tsang 1992)

$$k_f = \frac{d_H^2}{12}. \quad (2)$$

We also measure the volume of each model fracture, V_f. We vacuum the model fracture and then inject water into the fracture while the outlet valve is closed. The injection stops after the fracture is completely saturated with water. The volume of the fracture is estimated as the volume of water injected by the pump. The fracture volumes of Models A, B, and C are 14.2, 16.9, and 20.8 cm^3, respectively. We use these values in the calculation of aperture distribution.

A bending test of the fracture faces has also been performed by pressurizing the containing water up to 100 kPa. A micrometer (Peacock G-6C, Ozaki Manufacturing Company Limited, Tokyo, Japan; full scale: 1 mm, precision: 1 μm) is mounted on the model to measure the bending. In this study, all three model fractures are 4 cm thick. We house the fractures in aluminum frames. The maximum bending is 4 μm at the centroid of the fracture.

Characterization of Fracture Roughness and Geometry. In natural fractures, aperture varies, creating a 3D network of pore bodies and pore throats (Tsang 1984; Persoff et al. 1991; Rossen and Kumar 1992). In this study, we use a glass plate with one roughened side to represent the rough wall of a geological natural fracture. With the smooth glass plate, the roughened plate establishes a slit-like fracture channel between the two plates, with variable aperture. The roughened plates of all three model fractures in this study share the same roughness.

Fig. 3a shows the height topography of a 2 × 2-cm section of the roughened surface (resolution: 2,860 × 2,860, pixel size: 49 μm^2). The height data were profiled using a digital microscope (VHX-7000, Keyence, Osaka, Japan). The mean height value is 95 μm. The area-roughness parameters of the roughened plate S_a and S_q (arithmetical mean deviation and root mean squared of the height) are 38 and 45 μm, respectively.

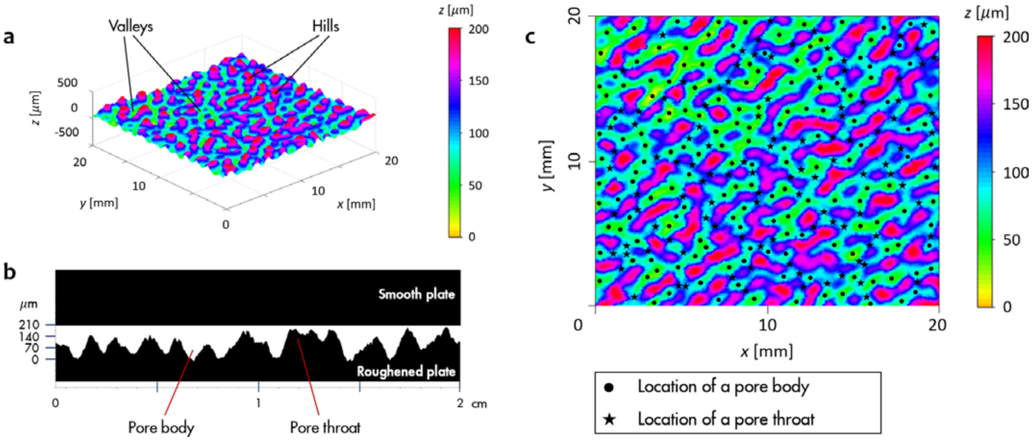

Fig. 3—(a) Height topography of the roughened plate. (b) Sketch of Model A. (c) 3D network of pore bodies and pore throats on the roughness.

The roughened surface can be characterized by connecting hills and valleys. Fig. 3b displays a sketch of Model A, where the hills and valleys of the roughened plate create a network of pore bodies and throats against the smooth plate. The scale of the height is greatly exaggerated in Fig. 3b.

For Model A, we put the smooth plate on top of the roughened plate; for Models B and C, strips of copper foils are placed between the two plates to increase the aperture. We then glue the two plates along the edges to create each model. Afterward, each model is clamped in an aluminum frame (Fig. 2). There is thus an extra gap between the two plates, caused by the fractionally penetrating glue and the copper foils. We estimate the gap, d', by comparing the fracture volume, V_f, determined from the volume of water required to fill the fracture, and the integral volume derived from the roughness distribution, V_r, which is given by Eq. 3,

$$V_r = \frac{L\, w}{A_p} \int_1^{2{,}860^2} (h_{\max} - h_i)\, dA_i, \quad (3)$$

where L is the length of the fracture, w is the width of the fracture, A_p is the size of the height topography (Fig. 3a), $h_{\max}$ is the maxima of the height data set, h_i is the height at each pixel, and A_i is the size of each pixel. The extra gap between the two plates of the model fractures is estimated by Eq. 4,

$$d' = \frac{V_f - V_r}{Lw}. \quad (4)$$

The d'-values of our three model fractures obtained from Eqs. 3 and 4 are 11, 23, and 67 μm, respectively. We combine d' and $(h_{\max} - h_i)$ to create the aperture distribution of each model fracture.

Foam behavior in the model fracture can be significantly affected by the geometry of the fracture (AlQuaimi and Rossen 2019b). To characterize the geometry of the model fractures, the typical apertures of the pore body and pore throat and the typical width of the pore throat are quantified. As shown in Fig. 3c, we define pore bodies at the local minima of height in the roughened surface. For each pore body, there might be multiple local minima, with only slightly different height, on the roughened plate; we combine these into one pore body. Pore throats, which connect pore bodies, are located at saddle points between pore bodies. We define the distance between positions of increasing height on either side of a saddle point as the width of the pore throat at that saddle point. **Table 1** shows the properties of our three model fractures. The throat/body-aperture ratio and aperture/width aspect ratio of the pore throat are also presented.

Fracture	Hydraulic Aperture, d_H (μm)	Fracture Volume, V_f (cm^3)	Permeability of Fracture, k_f (darcies)	Typical Pore-Throat Aperture, d_t (μm)	Typical Pore-Body Aperture, d_b (μm)	Typical Pore-Throat Width, w_t (μm)	Ratio of Throat Aperture to Body Aperture, $\frac{d_t}{d_b}$	Aspect Ratio of Pore Throat, $\frac{d_t}{w_t}$
Model A	78	14.2	507	92	174	762	0.53	0.12
Model B	98	16.9	800	110	192	762	0.57	0.14
Model C	128	20.8	1365	136	218	762	0.62	0.18

Table 1—Properties of Models A, B, and C.

Experiment Procedure and Image Analysis. Table 2 shows the eight experiments conducted in this study. We study foam by placing the fractures horizontally and sideways (turning the fracture on its long side). In particular, besides the sideways-flow experiment, we also place Model A vertically to study the effects of gravity on foam. In Experiment 2, we inject foam upward. Afterward, we turn the model over and perform Experiment 3 by injecting foam downward.

No.	Fracture	Hydraulic Aperture (μm)	Model Placement	Flow Direction
1	Model A	78	Horizontally	Horizontal
2			Vertically	Upward
3			Vertically	Downward
4			Sideways	Sideways
5	Model B	98	Horizontally	Horizontal
6			Sideways	Sideways
7	Model C	128	Horizontally	Horizontal
8			Sideways	Sideways

Table 2—Experiments conducted in this study.

In all experiments, a mixing tee (polyether ether ketone, Upchurch Scientific, Oak Harbor, Washington, USA) with a frit (mesh size: 10 μm) installed inside is used to pregenerate foam at a fixed foam quality (ratio of gas volumetric injection rate to total rate) f_g of 0.8, and at a fixed total interstitial velocity v_t of 1 mm/s. Foam quality and velocity are corrected based on the pressure at the middle of the fracture. The pregenerated foam then flows into the model fractures. The pregeneration step, combined with considerable foam coarsening by diffusion between the tee and entering the fracture, ensures that gas enters the fracture as relatively large bubbles instead of slugs. Foam texture is then further refined during flow within the model fracture. In this study, there is no backpressure at the outlet of the fracture. All experiments are conducted at 20°C and atmospheric pressure. Before each new foam experiment, the model fracture is thoroughly cleaned using demineralized water, then vacuumed and presaturated with surfactant solution for the next experiment.

Seven pressure transducers are used to measure the pressure of foam at different locations along the fracture (Fig. 2). We calculate the steady-state time-averaged pressure gradient ∇P_{foam} to quantify the strength of the steady-state foam. We also compute the standard deviation (SD) of steady-state pressure gradients to characterize the variability of our experimental results.

Images of foam in the model fractures are taken after the steady state of foam is reached. We use ImageJ software (Ferreira and Rasband 2012) to process and analyze the images. Properties of foam are thus quantified: The bubble density (number of bubbles/cm^2 of image) and bubble-size distribution are computed. The results are time- and location-averaged, meaning that images are taken at different times and also at different locations in each section after each experiment reaches steady state (Appendix A).

In Experiments 1, 2, and 3 on Model A, we program a macro to calculate the velocity of the gas-bubble train. Multiple time-lapse images during a 47-second period are processed. The macro identifies bubbles with a displacement greater than the average bubble diameter as flowing bubbles. The velocity of each flowing bubble is computed by the macro and is composed of a longitudinal (along the fracture) and a transverse vector (across the fracture). The transverse vector reflects the tortuosity of flow channels in the fracture. We estimate the velocity of the gas-bubble train as the average longitudinal velocity of all flowing bubbles. In addition, the area fraction of the trapped gas S'_g is estimated as

$$S'_g = \frac{A_{g,\,\text{trap}}}{A_{g,\,\text{total}}}, \quad (5)$$

where $A_{g,\text{trap}}$ is the area of the trapped gas and $A_{g,\text{total}}$ is the total area of gas. Eq. 5 is a 2D approximation of trapped-gas fraction. It provides a useful measure of gas trapping and for relating it to the effects of gravity and the hydraulic aperture of the fractures. The 2D gas-area fraction of the foam S_g^{2D} is further computed as

$$S_g^{2D} = \frac{A_{g,\text{total}}}{A_{\text{image}}}, \quad \ldots\ldots (6)$$

where A_{image} is the area of the image.

In sideways-flow experiments, we also calculate 3D gas saturation of foam at different heights of the fracture to study the effects of gravity. In the fracture with an uneven distribution of aperture, gas (trapped or flowing) tends to occupy locations of wider aperture. Liquid occupies areas with a tighter aperture in the model fracture. We plot the histogram of height data of the roughened plate and we compute the cumulative area fraction, by which we convert S_g^{2D} to gas saturation (Appendix B).

Using the correlation between the histogram of height on the surface and cumulative area fraction, we also estimate the aperture where gas/water interfaces are located around these water-filled locations for a specific gas-area fraction, d_a. We then estimate capillary pressure in the model fractures as

$$P_c = \frac{2\gamma_s \cos\theta}{d_a}, \quad \ldots\ldots (7)$$

where γ_s is the surface tension of the surfactant solution to air at 20°C. In this study, γ_s is measured to be 32.2 mN/m, using a tensiometer (Model SIGMA 701, KSV Instruments Ltd., Finland). θ is the contact angle. We assume that it is 0° because water completely wets the glass-model fractures.

Results and Discussion

Horizontal-Flow and Vertical-Flow Experiments in Model A. We conducted Experiment 1 in Model A by placing the model horizontally, where foam is not affected by gravity. **Fig. 4** shows bubble density, bubble size, and pressure gradient of the steady-state foam in different sections of the fracture.

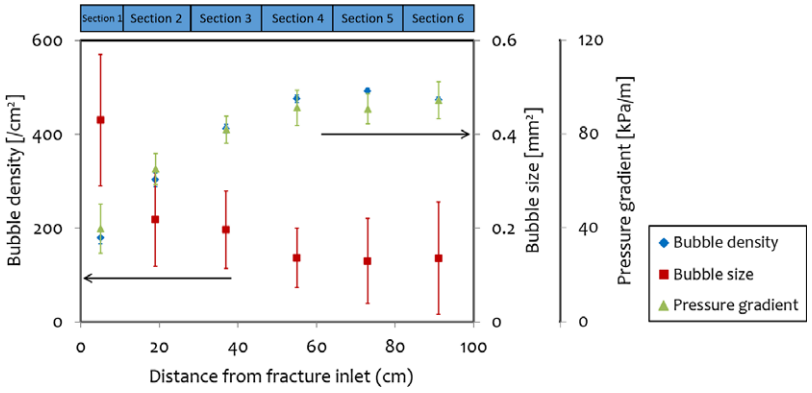

Fig. 4—Bubble density, bubble size, and pressure gradient of foam in different sections of Model A (d_{H_A} = 78 µm) in Experiment 1 (horizontal orientation). Vertical bars show the SD of our experimental results.

Although the mesh size of the frit in the mixing tee upstream of the model fracture is 10 µm, foam has coarsened into relatively large gas bubbles by the time it enters the fracture. As shown in Fig. 4, the bubble density increases and bubble size decreases along the fracture, indicating that the pregenerated foam is further refined as it propagates in the fracture. In this study, while injecting pregenerated foam, lamella division has been found to be the principal mechanism of foam generation inside the fracture (AlQuaimi and Rossen 2019a; Li et al. 2021). As a result of the finer and stronger foam, the pressure gradient also increases. In Experiment 1, we study foam at different times after foam reaches steady state to compute the SD of bubble density. We average the SD of bubble size in each section at different times. The large SD of bubble size indicates that foam bubbles in Model A are polydisperse. In the last three sections, the foam texture reaches a stable and constant state with bubble density of 481/cm^2 and bubble size of 0.135 mm^2. The pressure gradient is also the same in the last three sections at approximately 92 kPa/m. We conclude that foam has achieved LE in Model A (Ettinger and Radke 1992; Ashoori et al. 2010; Chen et al. 2010).

To study the effects of gravity, we place Model A vertically in Experiments 2 and 3. Before injecting foam, we clean the fracture with demineralized water and then vacuum and presaturate the fracture with the surfactant solution. Then we zero all seven pressure transducers, which means that measured pressures exclude the hydrostatic potential of the water in the fracture. **Fig. 5** shows how the measured pressure gradient evolves along the fracture for the three experiments. The upward-flooding Experiment 2 and downward-flooding Experiment 3 also reach LE in the last three sections, where the pressure gradient reaches a stable amplitude. The LE pressure gradients (averaged across the last three sections) of both experiments are close to that of the horizontal-flow experiment.

In the remainder of this paper, we examine foam in the last three sections where foam is at LE, unless otherwise indicated. We examine foam at different times and at different locations in the last three sections, where LE has been achieved, to compute the SD of LE foam properties. **Table 3** compares LE foam properties in Model A for Experiments 1, 2, and 3. In the vertical-flow experiments, Experiment 2 creates a finer-texture foam than Experiment 3. When the fracture stands vertically, water tends to accumulate in lower sections because of gravity. As a result, sections near the inlet of Experiment 2 are in a wetter state, which benefits in-situ foam generation (Rossen 1996). In contrast, in Experiment 3, the inlet is located at the top of the fracture, where a drier condition is present. Events of lamella creation are reduced because of relatively drier conditions. Despite the different foam texture between the upward-flooding and downward-flooding experiments, the LE pressure gradient (excluding the hydrostatic potential of water) is not significantly affected.

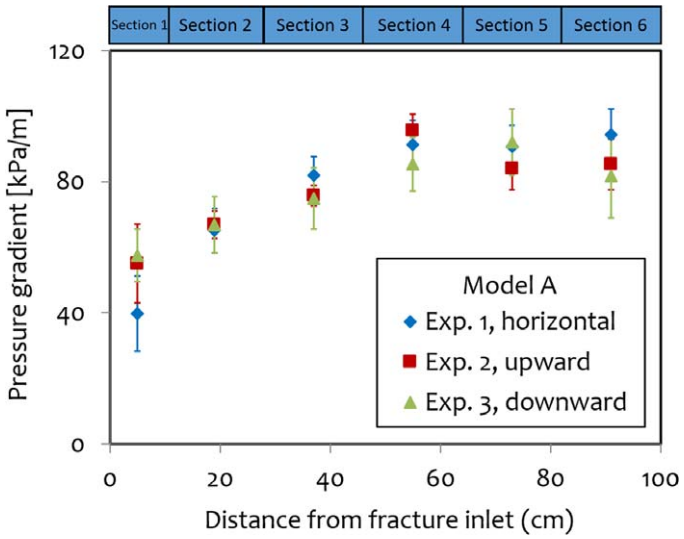

Fig. 5—Pressure gradient of Experiments 1, 2, and 3 in Model A ($d_{H_A} = 78\,\mu m$).

Experiment (Model A)	Pressure Gradient (kPa/m)	SD	Bubble Density (/cm^2)	SD	Bubble Size (mm^2)	SD	Gas Saturation (%)	SD	Trapped-Gas Fraction (%)	SD	Velocity of Bubble Trains (mm/s)
Experiment 1 (horizontal)	92.1	7.3	481	31	0.135	0.008	78.3	1.3	4.2	0.3	0.98
Experiment 2 (upward)	88.3	6.4	474	50	0.136	0.011	79.0	2.8	3.3	0.2	1.18
Experiment 3 (downward)	86.4	10.4	354	25	0.178	0.030	78.0	6.0	6.0	0.6	0.84

Table 3—Properties of LE foam of Experiments 1, 2, and 3 in Model A ($d_{H_A} = 78\,\mu m$).

The fact that the measured pressure gradient is similar in all three cases suggests that the potential gradient required for foam flow closely matches that of the water phase. On the other hand, one would expect a smaller potential gradient with larger bubbles (downward flow). The flow potential of a foam, with density less than that of water, might be somewhat less than that of water, reflected in our measured pressure differences. The combination of these two effects might explain why the measured pressure gradient for downward flow is so close to the other two values.

The trapped-gas fraction is also affected by gravity. Experiment 3 traps 6% of gas in pore bodies and Experiment 2 traps 3.3%. When foam flows downward in Experiment 3, the gravitational potential of gas (10 kPa/m), together with capillarity, hinders foam bubbles from flowing downward. In Experiment 2, the gravitational potential helps overcome the capillarity and moves bubbles upward, hence trapping less gas.

Despite the small trapped-gas fractions, the effect of gravity on the velocity of foam bubble trains is not significant. The velocities of bubble trains for three experiments are all close to 1 mm/s. The calculated velocity is number-averaged based on all flowing bubbles. In this foam, smaller bubbles that are much smaller than pore size propagate faster because of less resistance. For bubbles as large as (or larger than) pores, smaller bubbles would be expected to show greater resistance to flow (Falls et al. 1989). Although the velocity of bubble trains is computed from the number-averaged velocity for all moving bubbles, big or small, we believe that it provides a useful indication of the properties of the flowing gas fraction.

Gravity Segregation in Model A. In Experiment 4, we place Model A on its long side and inject foam sideways. **Fig. 6** shows that the pressure gradient of Experiment 4 is equivalent to Experiment 1, indicating that stable foam is also created in Experiment 4 when Model A stands on its side.

Fig. 7 shows bubble density and bubble size as a function of sections and heights of the fracture. Processed images of foam are shown in Appendix C. In sideways-flow experiments, we measure foam properties at the bottom, middle, and top, which are located at heights of 0, 7.5, and 15 cm of the fracture, respectively.

Fig. 7 shows that foam gets finer as it propagates in Model A. In Section 1, foam along the height of the fracture is uniform with properties similar to those in the horizontal-flow experiment (Fig. 4): bubble density of 180/cm^2 and bubble size of 0.43 mm^2. We inject the same pregenerated foam into the fracture in both horizontal-flow and sideways-flow experiments. In the last three sections, both bubble density and bubble size increase modestly with elevation within the fracture. This suggests that some foam bubbles flow toward the top of the fracture under gravity. **Fig. 8** shows gas saturation within the model. In sections near the inlet, gas saturation is also reasonably uniform along the height of the fracture. As foam propagates, some gravity segregation takes place: Drier foam flows at the top and wetter foam is at the bottom. In the last two sections, gas saturation is more than 10% drier than at the bottom.

Thus in Model A, foam is affected by gravity. Water and gas start to segregate as foam flows along the fracture. However, water and gas are not completely segregated in Model A (Appendix C). With an aperture of 78 μm and a height of 15 cm, foam is still in the capillary-transition zone in this fracture.

Effects of Hydraulic Aperture on Foam in Three Model Fractures. In an NFR, an open fracture can have an aperture of hundreds of microns or more (Luthi and Souhaite 1990). In this study, to examine foam in fractures with different apertures, we build three models with the same roughness and hydraulic apertures of 78, 98, and 128 μm, respectively. We conduct foam experiments on all three models by placing them horizontally. **Fig. 9** shows the pressure gradients of Experiments 1, 5, and 7 in Models A, B, and C. In all three model fractures, foam is stable and reaches LE in the last three sections, with a roughly uniform pressure gradient.

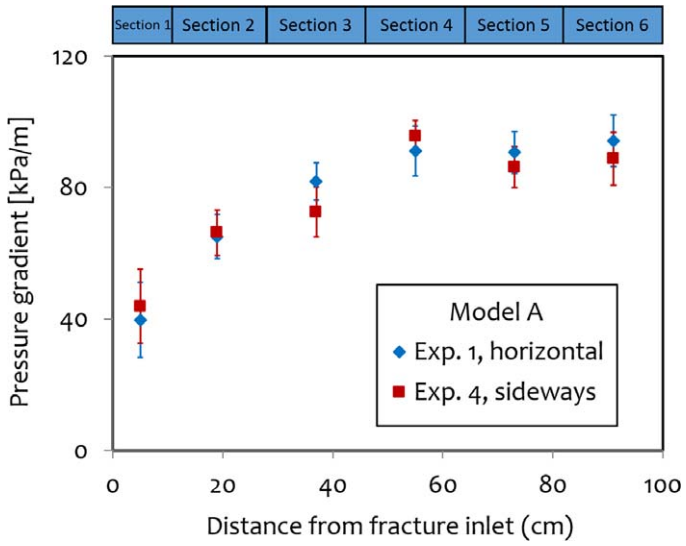

Fig. 6—Pressure gradient of Experiments 1 and 4 in Model A (d_{H_A} = 78 μm).

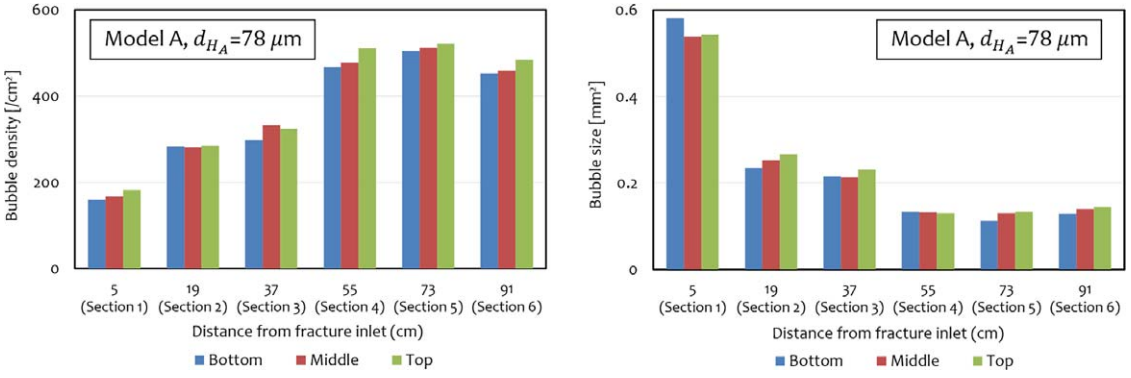

Fig. 7—(Left) Bubble density and (right) bubble size of foam in different sections and at different heights within Model A in Experiment 4 (sideways orientation).

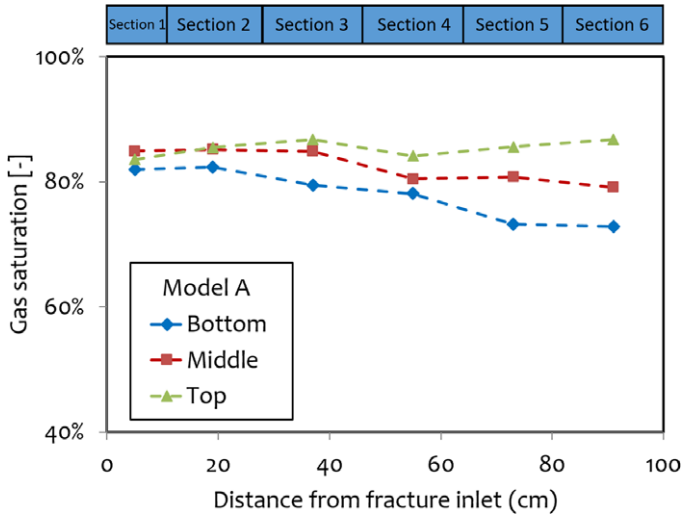

Fig. 8—Gas saturation of foam in different sections and at different heights of Model A (d_{H_A} = 78 μm) in Experiment 4 (sideways orientation).

As shown in Fig. 9, the pressure gradient decreases as the hydraulic aperture of the fracture increases from Model A to Model C, indicating a weakening foam. As the aperture increases, the curvature of lamellae passing through pore throats in the fracture becomes smaller. Thus, less viscous force is required to overcome the capillary force to move the foam bubbles.

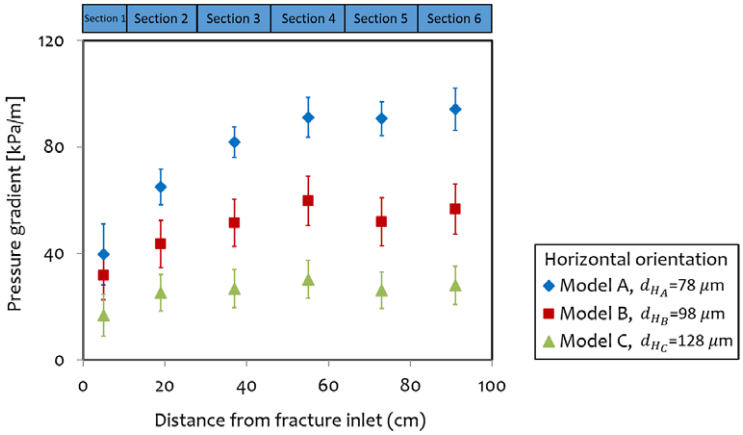

Fig. 9—Pressure gradient of Experiments 1, 5, and 7 in Models A, B, and C (horizontal orientation).

Table 4 displays foam properties of the three experiments. Foam is much coarser in models with a larger aperture. In our fractures, the pore throats are roughly in the shape of a slit. The aspect ratio of the pore throat, $\frac{d_t}{w_t}$, of the three model fractures in this study is 0.12, 0.14, and 0.18, respectively (Table 1). AlQuaimi and Rossen (2019a) argued that a smaller $\frac{d_t}{w_t}$ facilitates foam generation by snap-off at the throats. During initial drainage, more bubbles are also created in the fracture with a smaller throat/body-aperture ratio, $\frac{d_t}{d_b}$, because of the drop in capillary pressure as a gas/water interface advances from the throat to the body (Rossen 1996). During steady flow, a smaller fluctuation in local capillary pressure produces snap-off. Table 1 shows that both $\frac{d_t}{w_t}$ and $\frac{d_t}{d_b}$ increase from Model A to Model C. As the hydraulic aperture increases, less foam generation occurs, and thus there is coarser foam. The contrast in bubble volumes is greater than the contrast in areas shown in Table 4 because Model C has a larger aperture as well as a larger bubble area.

Experiment (Horizontal)	Hydraulic Aperture (μm)	Pressure Gradient (kPa/m)	SD	Bubble Density (/cm^2)	SD	Bubble Size (mm^2)	SD	Gas Saturation (%)	SD	Trapped-Gas Fraction (%)	SD
Experiment 1 (Model A)	78	92.1	7.3	481	31	0.135	0.008	78.3	1.3	4.2	0.3
Experiment 5 (Model B)	98	56.2	9.2	376	16	0.156	0.010	77.3	2.7	1.2	0.5
Experiment 7 (Model C)	128	28.2	7.0	200	6	0.313	0.021	79.3	2.1	0.0	0.0

Table 4—Properties of LE foam of Experiments 1, 5, and 7 in Models A, B, and C (horizontal orientation).

In Model C, the lamella density per unit of length is smaller due to a coarser foam compared with the other two models. The resistance on the foam flow is therefore reduced (Hirasaki and Lawson 1985). As a result, Model C creates the weakest foam with the lowest pressure gradient.

In addition, the trapped-gas fraction also decreases as the aperture increases. The throat/body-aperture ratio increases from Model A to Model C, signifying that the effect of capillary pressure on gas trapping is less pronounced. In Model C, there is no gas trapping. Viscous force dominates foam flow.

Gravity Segregation in Three Model Fractures. To further study the effects of gravity on foam, we conduct sideways-flow experiments in Models B and C by placing the model fractures on their long sides. **Table 5** compares foams in Section 2 of the fractures (near the inlet) for experiments with different fracture orientations. For both model fractures, in the sideways-flow experiment, the foam texture at different heights in Section 2 of the fracture is reasonably uniform, indicating that gravity effects on foam near the inlet are insignificant. In addition, foam texture in the sideways-flow experiment is similar to that in the horizontal-flow experiment, implying that we inject the same pregenerated foam into the fracture, despite the orientations.

Experiment	Hydraulic Aperture (μm)	Location Where Foam is Studied	Bubble Density (/cm^2)	Bubble Size (mm^2)
Experiment 5 (Model B, horizontal)	98	Section 2	284	0.238
		Bottom in Section 2	271	0.266
Experiment 6 (Model B, sideways)	98	Middle in Section 2	279	0.242
		Top in Section 2	291	0.249
Experiment 7 (Model C, horizontal)	128	Section 2	153	0.430
		Bottom in Section 2	141	0.455
Experiment 8 (Model C, sideways)	128	Middle in Section 2	151	0.439
		Top in Section 2	134	0.473

Table 5—Properties of foam in Section 2 of Models B and C in experiments with different fracture orientations.

Processed images of foam in different sections of Models B and C are shown in Appendix C. Bubble density and bubble size are also shown in Appendix C. **Fig. 10** shows average bubble density and bubble size of foam (averaged across the last three sections) at different heights of the three fractures.

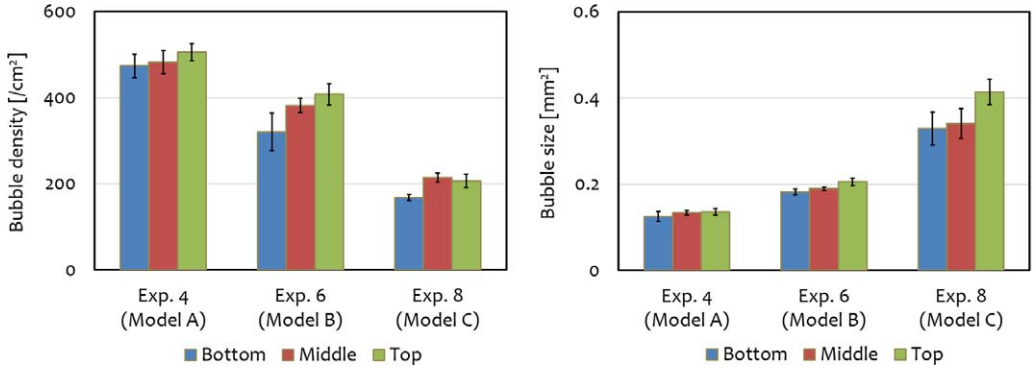

Fig. 10—(Left) Bubble density and (right) bubble size of foam (averaged across the last three sections) at different heights of Model A (d_{H_A} = 78 μm), Model B (d_{H_B} = 98 μm), and Model C (d_{H_C} = 128 μm) in Experiments 4, 6, and 8 (sideways orientation).

In Models A and B, bubble density of foam is greater at the top of the fractures. Foam bubbles tend to flow upward because of gravity in all three fractures, except Model C. However, the difference of bubble density along the height of Model C is not significant. This could reflect the 24% larger bubble area at the top of Model C than the middle and the bottom. The larger bubble area means fewer bubbles per unit area of the foam.

Fig. 11 shows gas saturation of foam in different sections and at different heights of Models B and C. As in Model A (Fig. 8), water and gas also segregate as foam propagates in Models B and C. As the hydraulic aperture increases from 78 to 98 to 128 μm, segregation increases along the fracture. As the aperture increases, the influence of the capillarity on the foam recedes. The effects of gravity increase, and as a result, gravity segregation is greater.

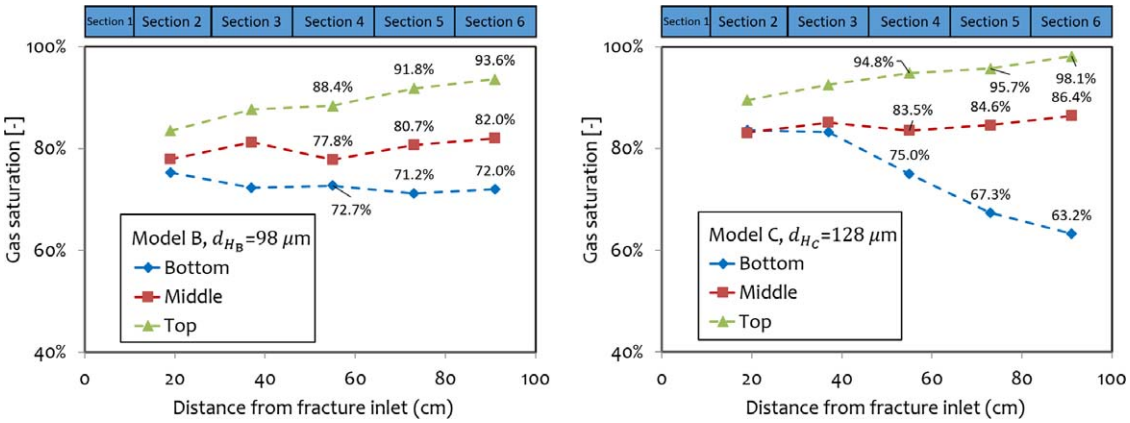

Fig. 11—Gas saturation of foam in different sections and at different heights of (left) Model B and (right) Model C in sideways orientation.

Fig. 12 compares gas saturation (averaged across the last three sections) at different heights of the three model fractures. In all three fractures, drier foam flows along the top of the fracture, and wetter foam at the bottom. The saturation at the top is 27.7, 19.3, and 10.8% greater than at the bottom for Models C, B, and A, respectively. Despite the gravity segregation in all three model fractures, water and gas are still not completely segregated either at the top or the bottom (Appendix C).

In all sideways-flow experiments, we did not observe significant bubble destruction by capillary coalescence. At the top of the fractures, the capillary pressure estimated from Eq. 7 is 1.12, 0.99, and 0.79 kPa for Models A, B, and C, respectively. The hydrostatic potential of a 15-cm-high water column is 1.47 kPa. Although foam is affected by gravity in all sideways-flow experiments (with greater segregation with increasing aperture), all three models represent a capillary-transition zone.

Discussion

In this paper, we have reported eight foam experiments in model fractures with different orientations. Each model in our study represents a single open geological fracture, with no flow interaction with the adjacent matrix. In horizontal-flow experiments with no gravity effects, foam gets coarser as hydraulic aperture increases. This seems to contradict the understanding of foam in porous media, where stronger foam is created in high-permeability zones. In porous media, capillary pressure would be much higher than what we estimated in our model fractures (Behrenbruch et al. 2016). In low-permeability zones in porous media, high capillary pressure restrains foam generation and accelerates coalescence. As a result, stronger foam created in high-permeability zones diverts gas into low-permeability zones. In our model fractures, foam is stable in all three model fractures, with much lower capillary pressure compared with porous media. In model fractures with larger hydraulic aperture, less in-situ foam generation takes place, thus creating a weaker foam. Despite

this fact, foam reaches LE in all three fractures. In addition, the pressure gradient seen in our horizontal-flow experiments (Fig. 9) suggests that foam similar to ours would benefit the diversion of gas from fractures into matrix in fractured reservoirs (Farajzadeh et al. 2010).

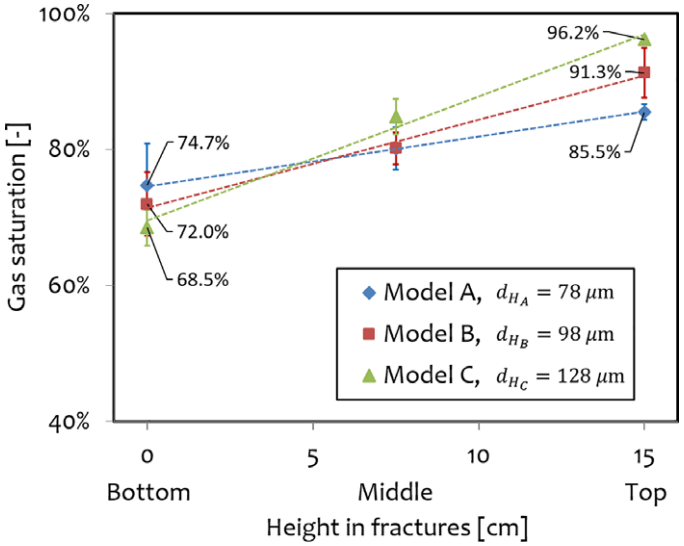

Fig. 12—Gas saturation (averaged across the last three sections) at different heights of Models A, B, and C in Experiments 4, 6, and 8 (sideways orientation).

In experiments with the model on its long side, we observed segregation in all three fractures. The segregation increases as foam flows through all our three model fractures. Our model fractures (1 m long and 15 cm wide) are much smaller in dimension than geological fractures in NFRs. The extent of gravity segregation seen in our study suggests that foam in vertical natural fractures (meters tall and tens of meters long, often with much greater aperture) is problematic. As a result of gravity segregation, the ability of foam to divert gas in a tall fracture over large distances will be weakened.

Skoreyko et al. (2012) developed a foam model to simulate gas-mobility control as a function of foam quality, foam degradation, regeneration, interfacial-tension reduction, and trapped gas in the naturally-fractured Cantarell Field. Using this model, they matched laboratory and field data to better understand foam application in fields. They also modeled gravity effects by correcting foam density as a function of foam quality. Luo et al. (2019) implemented a mechanistic foam model combining foam and microemulsion to history-match oil recovery and pressure drop of foam corefloods in a fractured oil-wet rock. The simulation results showed that pregenerated foam greatly resisted the fluid from flowing in the fracture near the injector and enhanced the diversion of injected fluids into the matrix.

As an initial study, the combined effects of gravity and aperture on foam reported in our paper suggest that gravity segregation or even complete separation of water and gas is a major issue in field application in tall vertical natural fractures over large distances. This thus needs to be taken into account in modeling. The implication of possible dry-out or collapse of foam in fractures needs to be further studied.

Conclusions

In this study, we report a series of experiments to investigate foam behavior in three model fractures with the same roughness on one face and different hydraulic apertures. Foam generation and destruction reach LE in the horizontal-flow experiments in all three model fractures and in the vertical-flow experiments in Model A. In the fracture with a larger hydraulic aperture, foam is coarser because of less in-situ foam generation. In both vertical-flow and sideways-flow experiments, foam is affected by gravity. In vertical-flow experiments with injection from the bottom, a finer-texture foam, with less gas trapping, is created, compared with injection from the top. In sideways-flow experiments, water and gas segregate to some extent as foam flows along the fracture: Drier foam flows along the top of the fracture, and wetter foam along the bottom. The segregation is greater as hydraulic aperture increases; gravity becomes more influential as capillary effects weaken with larger aperture. In this study, foam is affected by gravity in model fractures with an aperture up to 128 μm. All three models represent a capillary-transition zone, with greater segregation with increasing aperture. The extent of gravity segregation seen in our experiments suggests that foam in vertical natural fractures (meters tall and tens of meters long, often with much greater aperture) is problematic and could impair the capacity of foam to divert gas flow in a tall fracture over large distances.

Nomenclature

$A_{g,\text{total}}$ = total area of gas from image analysis, mm^2
$A_{g,\text{trap}}$ = area of trapped gas from image analysis, mm^2
A_i = size of each pixel, μm^2
A_{image} = area of the image, mm^2
A_p = size of the height topography, m^2
d_a = aperture at where gas/water interface locates for a specific gas-area fraction, μm
d_b = typical aperture of pore body, μm
d_H = hydraulic aperture of the model fracture, μm
d_{H_A}, d_{H_B}, d_{H_C} = hydraulic aperture of Models A, B, and C, μm
d_t = typical aperture of pore throat, μm
$\frac{d_t}{d_b}$ = throat/body-aperture ratio

$\frac{d_t}{w_t}$ = aspect ratio of the pore throat
d' = extra gap between two plates of the model, μm
f_g = foam quality (i.e., the ratio of gas volumetric injection rate to total rate)
h_i = height at each pixel, μm
$h_{\max}$ = maxima of the height data set, μm
k_f = hydraulic permeability of fracture, darcies
L = length of the model fracture, m
P_c = capillary pressure, kPa
q_w = volumetric water-injection rate, cm^3/min
S_a = area-roughness parameter: arithmetical mean deviation of the height of the roughened plate, μm
S_g = gas saturation of foam, %
S_g^{2D} = gas-area fraction, %
S_g' = area fraction of trapped gas, %
S_q = area-roughness parameter: root mean squared of the height of the roughened plate, μm
v_t = total interstitial velocity, mm/s
V_f = fracture volume, cm^3
V_r = integral volume brought forth by the roughness, cm^3
w = width of the model fracture, m
w_t = typical width of pore throat, μm
γ_s = surface tension of the surfactant solution to air at 20°C, mN/m
θ = contact angle, degrees
μ_w = viscosity of water, mPa·s
∇P_{foam} = pressure gradient of steady-state foam flow, kPa/m
∇P_w = pressure gradient upon water injection, kPa/m

Acknowledgments

This study is a part of the Joint Industry Project on Foam for Enhanced Oil Recovery. We thank Shell, Equión, Engie, ConocoPhillips, and Pemex for funding this study. We also thank Michiel Slob and Joost van Meel in the Geo-Energy & Geoscience and Engineering Laboratory at Delft University of Technology, The Netherlands, for their technical support.

References

AlQuaimi, B. I. and Rossen, W. R. 2019a. Foam Generation and Rheology in a Variety of Model Fractures. *Energy Fuels* **33** (1): 68–80. https://doi.org/10.1021/acs.energyfuels.8b02178.

AlQuaimi, B. I. and Rossen, W. R. 2019b. Study of Foam Generation and Propagation in Fully Characterized Physical-Model Fracture. *J Pet Sci Eng* **175** (April): 1169–1181. https://doi.org/10.1016/j.petrol.2018.06.025.

Ashoori, E., Marchesin, D., and Rossen, W. R. 2010. Roles of Transient and Local Equilibrium Foam Behavior in Porous Media–Traveling Wave. Paper presented at ECMOR XII-12th European Conference on the Mathematics of Oil Recovery, Oxford, UK, 6–9 September. https://doi.org/10.3997/2214-4609.20144931.

Behrenbruch, P., Huu, M. T. D., Hoang, T. G. et al. 2016. Modelling of Drainage Capillary Pressure: A Comparative Study of Various Analytical Capillary Pressure Formulations in Matching Laboratory Results. Paper presented at the SPE Asia Pacific Oil and Gas Conference and Exhibition, Perth, Australia, 25–27 October. SPE-182469-MS. https://doi.org/10.2118/182469-MS.

Brattekås, B., Eide, Ø., Johansen, S. A. et al. 2020. Foam Flow and Mobility Control in Natural Fracture Networks. *Transp Porous Media* **131** (1): 157–174. https://doi.org/10.1007/s11242-019-01249-3.

Chen, Q., Gerritsen, M. G., and Kovscek, A. R. 2010. Modeling Foam Displacement with the Local-Equilibrium Approximation: Theory and Experimental Verification. *SPE J*. **15** (1): 171–183. SPE-116735-PA. https://doi.org/10.2118/116735-PA.

Ettinger, R. A. and Radke, C. J. 1992. Influence of Texture on Steady Foam Flow in Berea Sandstone. *SPE Res Eng* **7** (1): 83–90. SPE-19688-PA. https://doi.org/10.2118/19688-PA.

Falls, A. H., Musters, J. J., and Ratulowski, J. 1989. The Apparent Viscosity of Foams in Homogeneous Bead Packs. *SPE Res Eng* **4** (2): 155–164. SPE-16048-PA. https://doi.org/10.2118/16048-PA.

Farajzadeh, R., Wassing, B., and Boerrigter, P. 2010. Foam Assisted Gas Oil Gravity Drainage in Naturally-Fractured Reservoirs. Paper presented at the SPE Annual Technical Conference and Exhibition, Florence, Italy, 19–22 September. SPE-134203-MS. https://doi.org/10.2118/134203-MS.

Fernø, M. A., Gauteplass, J., Pancharoen, M. et al. 2016. Experimental Study of Foam Generation, Sweep Efficiency, and Flow in a Fracture Network. *SPE J*. **21** (4): 1140–1150. SPE-170840-PA. https://doi.org/10.2118/170840-PA.

Ferreira, T. and Rasband, W. 2012. Image J User Guide. ImageJ/Fiji, 155–161.

Hirasaki, G. J. and Lawson, J. B. 1985. Mechanisms of Foam Flow in Porous Media: Apparent Viscosity in Smooth Capillaries. *SPE J*. **25** (2): 176–190. SPE-12129-PA. https://doi.org/10.2118/12129-PA.

Hirasaki, G. J., Miller, C. A., Szafranski, R. et al. 1997. Surfactant/Foam Process for Aquifer Remediation. Paper presented at the International Symposium on Oilfield Chemistry, Houston, Texas, USA, 18–21 February. SPE-37257-MS. https://doi.org/10.2118/37257-MS.

Katiyar, A., Patil, P. D., Rohilla, N. et al. 2019. Industry-First Hydrocarbon-Foam EOR Pilot in an Unconventional Reservoir: Design, Implementation, and Performance Analysis. Paper presented at the SPE/AAPG/SEG Unconventional Resources Technology Conference, Denver, Colorado, USA, 22–24 July. URTEC-2019-103-MS. https://doi.org/10.15530/urtec-2019-103.

Kovscek, A. R. and Radke, C. J. 1994. Fundamentals of Foam Transport in Porous Media. In *Foams: Fundamentals and Applications in the Petroleum Industry*, Vol. 242, ed. L. L. Schramm, 115–163. Washington, DC, USA: American Chemical Society.

Li, K., Wolf, K. A. A., and Rossen, W. R. 2021. Effects of Gas Trapping on Foam Mobility in a Model Fracture. *Transp Porous Media* **138** (1): 185–200. https://doi.org/10.1007/s11242-021-01598-y.

Luo, H., Mateen, K., Ma, K. et al. 2019. In-Depth Understanding of the Ultra-Low-Interfacial-Tension Foam Flood in Oil-Wet Fractured Media through Simulation with an Integrative Mechanistic Foam Model. Paper presented at the SPE Annual Technical Conference and Exhibition, Calgary, Alberta, Canada, 30 September–2 October. SPE-196123-MS. https://doi.org/10.2118/196123-MS.

Luthi, S. M. and Souhaite, P. 1990. Fracture Apertures from Electrical Borehole Scans. *Geophysics* **55** (7): 821–833. https://doi.org/10.1190/1.1442896.

Ocampo, A., Restrepo, A., Clavijo, J. et al. 2020. Successful Foams EOR Field Pilot in a Naturally Fractured Reservoir by the Injection of the Foaming Agent Dispersed in the Gas Stream. Paper presented at the SPE Improved Oil Recovery Conference, Virtual, 31 August–4 September. SPE-200377-MS. https://doi.org/10.2118/200377-MS.

Patzek, T. W. 1996. Field Applications of Steam Foam for Mobility Improvement and Profile Control. *SPE Res Eng* **11** (2): 79–86. SPE-29612-PA. https://doi.org/10.2118/29612-PA.

Persoff, P. and Pruess, K. 1995. Two-Phase Flow Visualization and Relative Permeability Measurement in Natural Rough-Walled Rock Fractures. *Water Resour Res* **31** (5): 1175–1186. https://doi.org/10.1029/95WR00171.

Persoff, P. G., Pruess, K., and Myer, L. 1991. Two-Phase Flow Visualization and Relative Permeability Measurement in Transparent Replicas of Rough-Walled Rock Fractures. Paper presented at the 16th Workshop on Geothermal Reservoir Engineering, Stanford, California, USA, 23–25 January.

Rossen, W. R. 1996. Foams in Enhanced Oil Recovery. In *Foams: Theory, Measurements, and Applications*, Vol. 57, ed. R. K. Prud'homme and S. Khan, 413–464. Boca Raton, Florida, USA: CRC Press.

Rossen, W. R. and Kumar, A. T. 1992. Single-and Two-Phase Flow in Natural Fractures. Paper presented at the SPE Annual Technical Conference and Exhibition, Washington, DC, USA, 4–7 October. SPE-24915-MS. https://doi.org/10.2118/24915-MS.

Skoreyko, F. A., Villavicencio, A. P., Rodriguez Prada, H. et al. 2012. Understanding Foam Flow with a New Foam EOR Model Developed from Laboratory and Field Data of the Naturally Fractured Cantarell Field. Paper presented at the SPE Improved Oil Recovery Symposium, Tulsa, Oklahoma, USA, 14–18 April. SPE-153942-MS. https://doi.org/10.2118/153942-MS.

Stearns, D. W. and Friedman, M. 1972. Reservoirs in Fractured Rock. In *Stratigraphic Oil and Gas Fields—Classification, Exploration Methods, and Case Histories*, Vol. 16, ed. R. E. King, 82–106. Tulsa, Oklahoma, USA: American Association of Petroleum Geologists.

Tang, G. Q. and Kovscek, A. R. 2006. Trapped Gas Fraction during Steady-State Foam Flow. *Transp Porous Media* **65** (2): 287–307. https://doi.org/10.1007/s11242-005-6093-4.

Thompson, K. E. and Gdanski, R. D. 1993. Laboratory Study Provides Guidelines for Diverting Acid with Foam. *SPE Prod & Fac* **8** (4): 285–290. SPE-23436-PA. https://doi.org/10.2118/23436-PA.

Tsang, Y. W. 1984. The Effect of Tortuosity on Fluid Flow through a Single Fracture. *Water Resour Res* **20** (9): 1209–1215. https://doi.org/10.1029/WR020i009p01209.

Tsang, Y. W. 1992. Usage of "Equivalent Apertures" for Rock Fractures as Derived from Hydraulic and Tracer Tests. *Water Resour Res* **28** (5): 1451–1455. https://doi.org/10.1029/92WR00361.

van Golf-Racht, T. D. 1982. *Fundamentals of Fractured Reservoir Engineering*, Vol. 12, first edition. New York, New York, USA: Developments in Petroleum Science Series, Elsevier.

Witherspoon, P. A., Wang, J. S., Iwai, K. et al. 1980. Validity of Cubic Law for Fluid Flow in a Deformable Rock Fracture. *Water Resour Res* **16** (6): 1016–1024. https://doi.org/10.1029/WR016i006p01016.

Appendix A—Locations Where Images are Taken

In this study, we examine foam by image analysis. As shown in **Fig. A-1,** we take multiple images at different times and different locations in each section on the model fracture after each experiment reaches steady state. The calculated foam properties are time- and location-averaged.

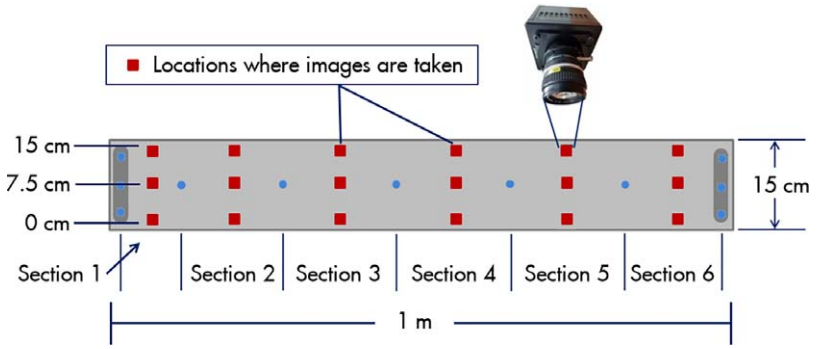

Fig. A-1—Setup of the model fracture and the camera. Images are taken at locations shown as red squares on the fracture.

Appendix B—Conversion of Gas-Area Fraction to Gas Saturation

As shown in **Fig. B-1,** to convert the gas-area fraction to gas saturation, the histogram of heights of the roughened plate is studied, by which the cumulative area fraction is computed. In this study, the fractures have an uneven distribution of aperture (Fig. 3). During foam flooding, gas tends to occupy locations of wider aperture, and liquid occupies areas with tighter aperture in the model fracture. We integrate the product of height and area fraction at that height to compute gas saturation from area fraction for our three models. This also requires an estimate of the position of the smooth glass plate relative to the roughened one, based on the measurement of liquid volume in the fully saturated model. Our estimate does not include liquid in the Plateau borders along lamellae between foam bubbles.

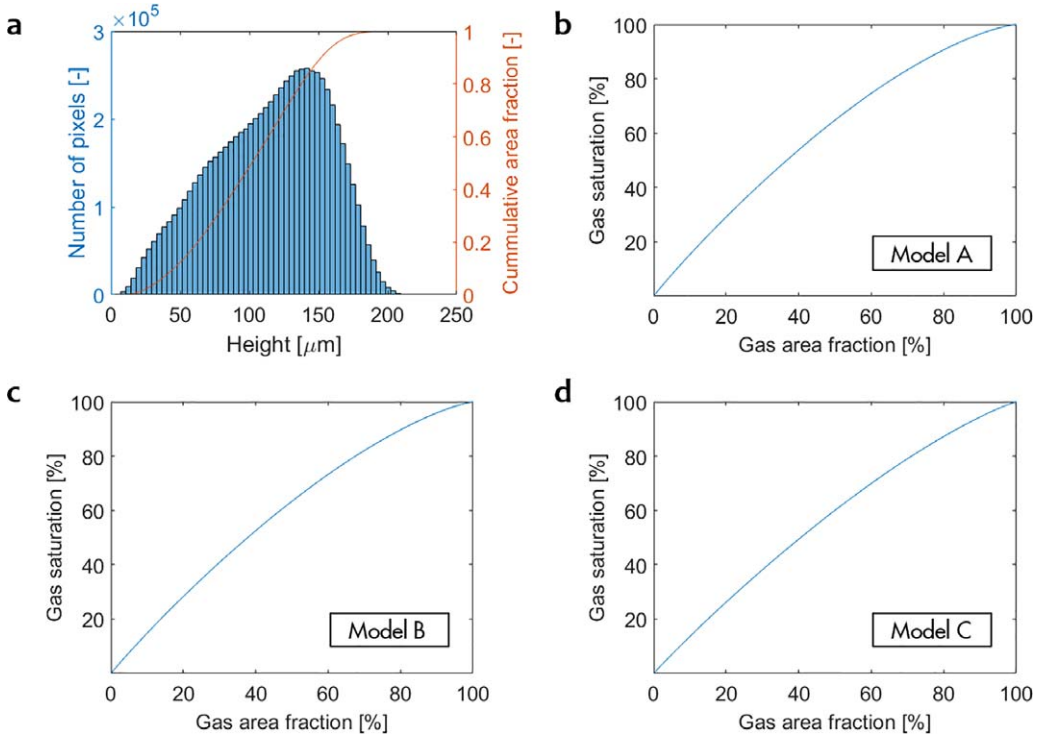

Fig. B-1—(a) Histogram of height data of the roughened plate and cumulative area fraction. (b) Conversion of gas-area fraction to gas saturation for Model A (d_{H_A} = 78 μm). (c) Conversion of gas-area fraction to gas saturation for Model B (d_{H_B} = 98 μm). (d) Conversion of gas-area fraction to gas saturation for Model C (d_{H_C} = 128 μm).

Appendix C—Processed Images and Properties of Foam in Sideways-Flow Experiments

Figs. C-1 and **C-2** show processed images of foam in different sections and at different heights of Models A (Fig. C-1), B, and C (Fig. C-2) in sideways orientation. These images are representative of multiple images taken in the same locations and at different times.

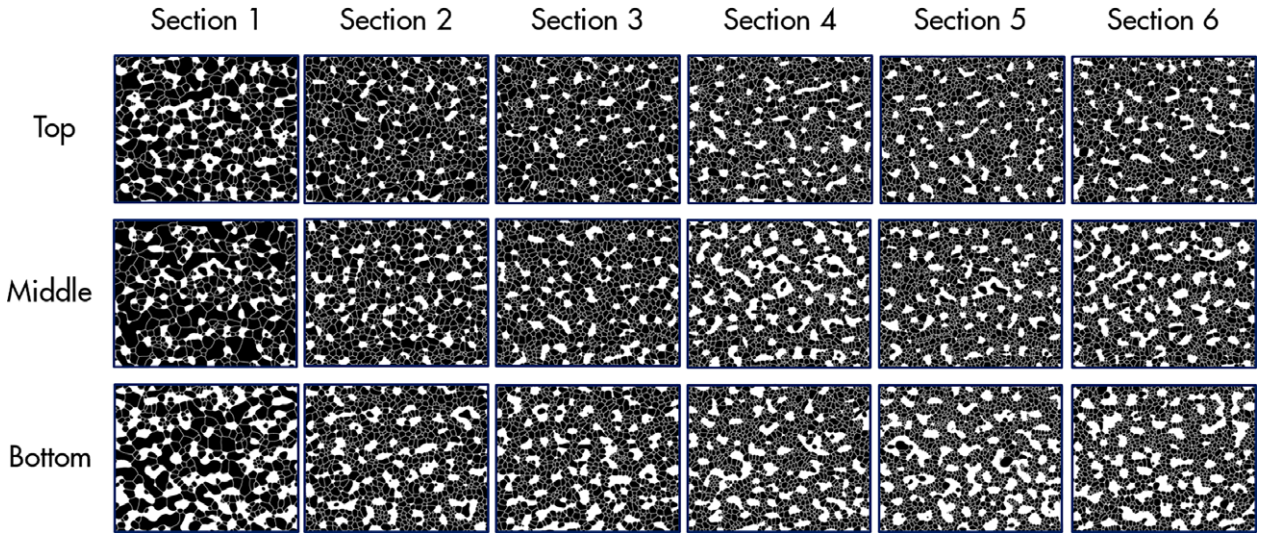

Fig. C-1—Processed images of foam in different sections and at different heights of Model A (d_{H_A} = 78 μm) in sideways orientation. Images are taken at locations shown as red squares on the fracture in Fig. A-1. Gas is shown in black, liquid in white. Liquid occupies areas with tighter aperture in the model fracture. Image size: 1.95 × 1.56 cm.

Figs. C-3 and **C-4** show the bubble density and bubble size of foam in different sections and at different heights of Models B (Fig. C-3) and C (Fig. C-4) in sideways orientation.

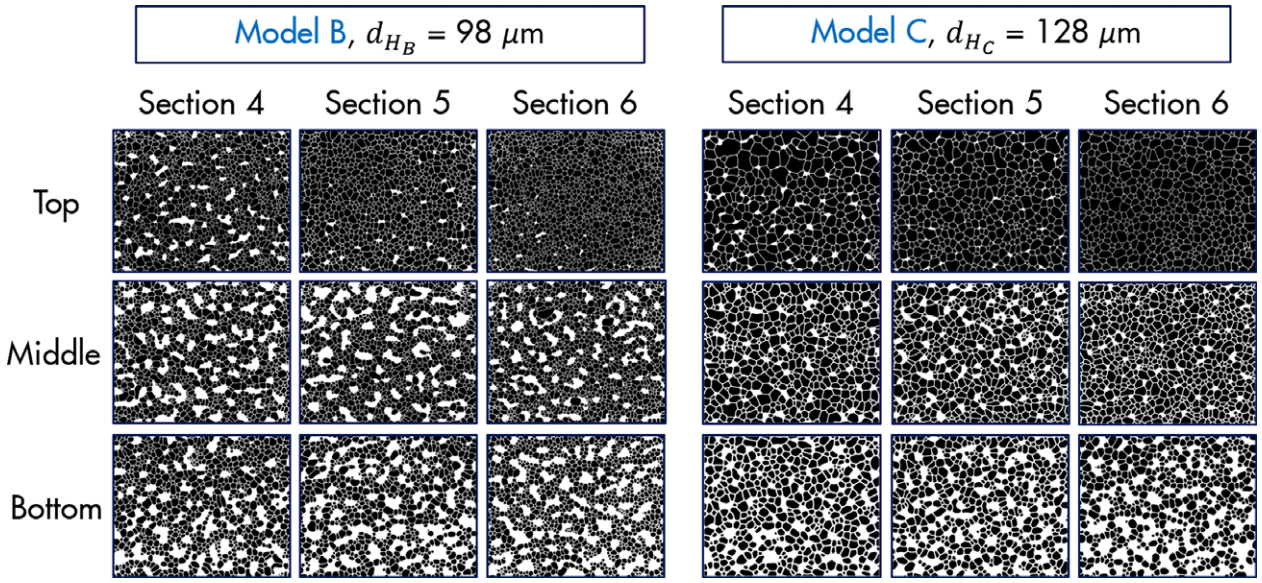

Fig. C-2—Processed images of foam in different sections and at different heights of Model B with d_{H_B} = 98 μm (left) and Model C with d_{H_C} =128 μm (right) in sideways orientation. Gas is shown in black, liquid in white. Liquid occupies areas with tighter aperture in the model fracture. Image size: 1.95 × 1.56 cm.

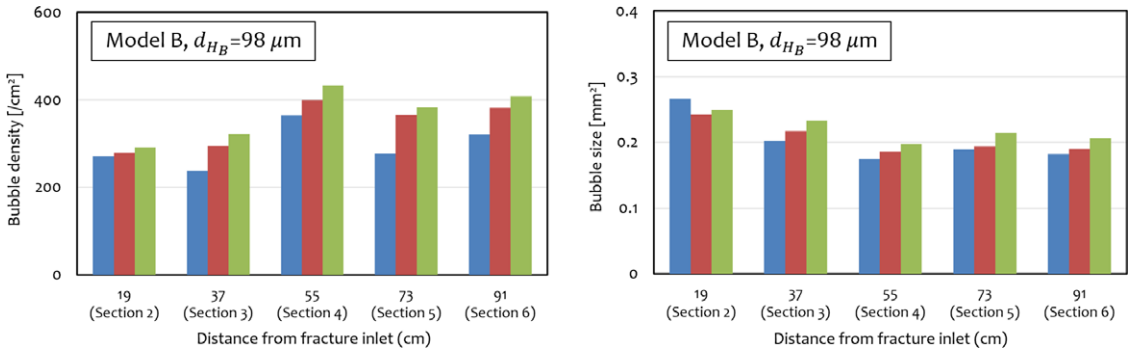

Fig. C-3—(Left) Bubble density and (right) bubble size of foam in different sections and at different heights within Model B in Experiment 6 (sideways orientation).

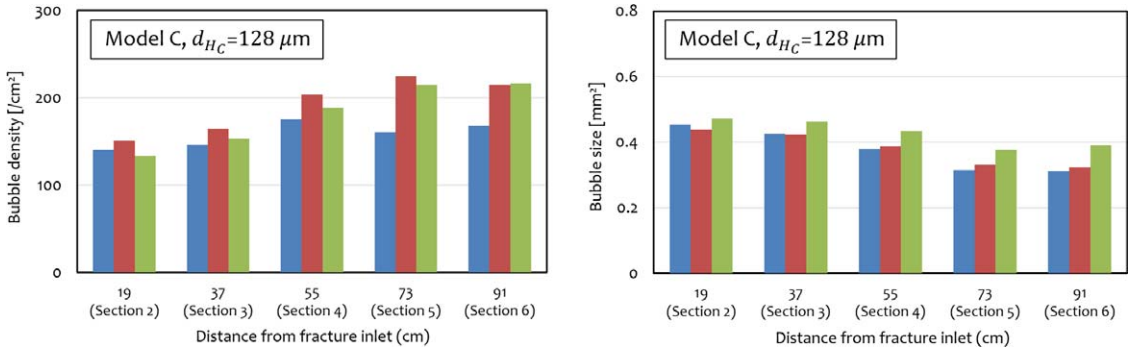

Fig. C-4—(Left) Bubble density and (right) bubble size of foam in different sections and at different heights within Model C in Experiment 8 (sideways orientation).